NMR structure and dynamics of monomeric neutrophil-activating peptide 2

Helen YOUNG*, Vikram ROONGTA*, Thomas J. DALY†[2] and Kevin H. MAYO*[1]

*Department of Biochemistry, Biomedical Engineering Center, University of Minnesota, 435 Delaware Street, S.E., Minneapolis, MN 55455, U.S.A., and †Repligen Corporation, One Kendall Square, Building 700, Cambridge, MA 02139, U.S.A.

Neutrophil-activating peptide 2 (NAP-2), which demonstrates a range of proinflammatory activities, is a 72-residue protein belonging to the α-chemokine family. Although NAP-2, like other α-chemokines, is known to self-associate into dimers and tetramers, it has been shown that the monomeric form is physiologically active. Here we investigate the solution structure of monomeric NAP-2 by multi-dimensional ^{1}H-NMR and ^{15}N-NMR spectroscopy and computational modelling. The NAP-2 monomer consists of an amphipathic, triple-stranded, anti-parallel β-sheet on which is folded a C-terminal α-helix and an aperiodic N-terminal segment. The backbone fold is essentially the same as that found in other α-chemokines. ^{15}N T_1, T_2 and nuclear Overhauser effects (NOEs) have been measured for backbone NH groups and used in a model free approach to calculate order parameters and conformational exchange terms that map out motions of the backbone. N-terminal residues 1 to 17 and the C-terminus are relatively highly flexible, whereas the β-sheet domain forms the most motionally restricted part of the fold. Conformational exchange occurring on the millisecond time scale is noted at the top of the C-terminal helix and at proximal residues from β-strands 1 and 2 and the connecting loop. Dissociation to the monomeric state is apparently responsible for increased internal mobility in NAP-2 compared with dimeric and tetrameric states in other α-chemokines.

Key words: chemokine, internal motions, protein.

INTRODUCTION

Neutrophil-activating peptide 2 (NAP-2) [1], low-affinity platelet factor 4 (LA-PF4) [2] [also named connective-tissue-activating protein III (CTAP-III) [3]] and β-thromboglobulin (βTG) [4] are platelet-specific, naturally occurring N-terminal cleavage products of platelet basic protein (PBP) [2]. All are homologues of platelet factor 4 (PF4) [5] and are members of the growing family of C-X-C proteins or α-chemokines [6], which include interleukin 8 (IL-8) [1,7] and Gro-α [8]. Collectively, this protein family is involved in inflammation, blood clotting and wound healing.

NAP-2 is exceptionally potent at neutrophil activation and acts like homologous IL-8 in neutrophil chemotaxis [9]; it competes with IL-8 for binding to neutrophil cell-surface IL-8 receptors and subsequent G-protein activation [10,11]. Because NAP-2 devoid of its C-terminal segment is at least partly biologically active, the NAP-2 N-terminal domain, which includes the N-terminus and topologically related residues, apparently possesses the neutrophil activation properties [12]. Even though NAP-2 at millimolar concentrations exists in solution as an equilibrium between monomeric, dimeric and tetrameric states [13], like PF4 [14], it is primarily monomeric under physiological conditions, in which its concentration is considerably lower [13,15]. However, at nanomolar concentrations, at which NAP-2 induces changes in cytosolic free [Ca^{2+}] and neutrophil chemotaxis and exocytosis, it certainly must be monomeric. In support of our original proposal that α-chemokines such as NAP-2 are probably active as monomers [15], Rajarathnam et al. [16,17] synthesized monomeric forms of IL-8, NAP-2 and melanoma growth stimulatory activity (MGSA) and showed that these α-chemokines are indeed active as monomers. In this respect, the study of the NAP-2 monomer state is most relevant to developing structure–function relationships and understanding how this chemokine functions biologically. Although the X-ray crystal structure of tetrameric NAP-2 is known [18], the present NMR study provides an added dimension by addressing the solution structure and motional dynamics of monomeric NAP-2 in the absence of conformationally stabilizing/modifying subunit associations.

In previous NMR studies of NAP-2 [13,19], the self-association-induced exchange broadening of resonances and the presence of multiple aggregate states were overcome by using various agents (salts and organic compounds) to disaggregate NAP-2. The most effective of these is 2-chloroethanol [20], which at low concentration [3–4 % (v/v)] essentially dissociates NAP-2 to the monomeric state [19]. This allowed most ^{1}H sequence-specific assignments to be made for monomeric NAP-2 and secondary structural elements to be deduced from a qualitative interpretation of ^{1}H nuclear Overhauser effects (NOEs), $^3J_{\alpha N}$ coupling constants and long-lived backbone NH groups [19]. As with other α-chemokines whose structures are known (e.g. PF4 [21–23], IL-8 [24] and SDF-1 [25]), monomeric NAP-2 contains a triple-stranded anti-parallel β-sheet with strand 2 (residues 34–41) hydrogen-bonded to strands 1 (residues 22–28) and 3 (residues 46–49). Strands 1 and 2 are connected by a loop that is folded proximally to the neutrophil-activating N-terminal tripeptide sequence Glu-Leu-Arg. An α-helix extends from residue 55 to the C-terminus, with the last five C-terminal residues being undefined by the data. In that ^{1}H-NMR study [19], structural modelling could not be completed owing to a lack of key long-range NOEs that were required to position the C-terminal α-

Abbreviations used: 2D, two-dimensional; 3D, three-dimensional; IL-8, interleukin 8; HMQC, heteronuclear multiple quantum coherence; HOHAHA, homonuclear Hartman–Hahn spectroscopy; NAP-2, neutrophil-activating peptide 2; NOE, nuclear Overhauser effect; PF4, platelet factor 4; RMS, root-mean-square; TPPI, time-proportional phase incrementation.

[1] To whom correspondence should be addressed (e-mail mayox001@maroon.tc.umn.edu).

[2] Present address: Regeneron, Inc., Tarrytown, NY 10591, U.S.A.

helix with respect to the β-sheet. In the present study, recombinant NAP-2 was uniformly enriched in ^{15}N, and ^{15}N-edited two-dimensional (2D) and three-dimensional (3D) NMR experiments permitted a detailed structural analysis. In addition, ^{15}N-{^1H} T_1, T_2 and NOE relaxation terms were acquired and used to derive backbone motional parameters. The motional study, in particular, provides a unique understanding of the physical state of monomeric NAP-2.

MATERIALS AND METHODS

Isolation of recombinant NAP-2

The synthetic gene for human NAP-2 was expressed as a non-fusion protein in *Escherichia coli* (BL21) cells and grown on a 10-litre scale. NAP-2 was purified, cleaved and refolded essentially as described previously [26]. Purity was assessed by Coomassie staining of SDS/PAGE gels, analytical C_4 reverse-phase HPLC and amino acid analysis. Typically, several hundred milligrams of material that was more than 95% pure were isolated from 100 g of starting material. Protein concentration was determined by using the bicinchoninic acid assay [27].

NMR spectroscopy

Samples for ^1H-NMR measurements were freeze-dried and redissolved in ^1H_2O or ^2H_2O immediately before the experiment. For work in ^1H_2O solutions, 10% (v/v) ^2H_2O was routinely used. The solution also contained 4% (v/v) perdeuterated 2-chloroethanol to dissociate dimer–tetramer aggregate states [19,20]. The final protein concentration was 18 mg/ml. The pH was adjusted to pH 3.6 by adding microlitre increments of NaO^{2}H or ^{2}HCl to a 0.6 ml sample. The pH was not adjusted for isotope effects. Most experiments were acquired at 313 K. NMR spectra were recorded in the Fourier mode on a Bruker AMX-600 or on Varian Inova Unity Plus-500 and/or Varian Inova Unity Plus-600 spectrometers. The ^2H_2O deuterium signal was used as a field-frequency lock. All chemical shifts are quoted in parts per million (p.p.m.) downfield of sodium 2,2-dimethyl-2-silapentane sulphonate.

Sequence-specific assignments for most ^1H resonances of NAP-2 have been reported by Mayo et al. [19] from analysis of COSY, double-quantum-filtered COSY, homonuclear Hartman–Hahn spectroscopy (HOHAHA) and NOESY experiments. Heteronuclear ^1H–^{15}N NMR experiments have been done in this paper to provide ^{15}N and complete ^1H resonance assignments as well as to acquire additional NOE constraints for computational modelling and backbone dynamics studies.

2D-NMR and 3D-NMR ^1H–^{15}N heteronuclear multiple quantum coherence (HMQC)-HOHAHA and NOESY [28–31] experiments were acquired to assign ^{15}N resonances. The water signal was suppressed by using direct irradiation or square pulses (100 ms for 0.6 s) of 1024 points especially for the ^1H–^{15}N spectra. The mixing time on ^1H–^{15}N HMQC-HOHAHA experiments was 60 ms. HMQC-NOESY experiments were acquired by using mixing times of 50, 75, 100 and 200 ms. The ^1H carrier was placed at the water frequency or in the centre of the ^{15}N–^1H region, with ^{15}N carrier at 125.0 p.p.m. The acquired data matrices for each 2D experiment were 512 (t_1) × 1024 (t_2) complex data points, with spectral widths of 7200 Hz in F_1(^1H) and 3600 Hz in the F_2 dimension of ^{15}N. Spectra were recorded in the pure absorption mode by using the time-proportional phase incrementation (TPPI) and TPPI-states methods for quadrature detection in t_1 and t_2 respectively. Zero-filling and linear prediction were employed to yield spectra of 1024 (F_1) × 1024 (F_2) points. The acquired data matrices for each 3D experiment were 128 (t_1) × 32 (t_2) × 1024 (t_3) complex data points, with spectral widths of 7200, 3600 and 7200 Hz in the F_1(^1H), F_2(^{15}N) and F_3(^1H) dimensions respectively. The spectra were recorded in pure absorption mode by using the TPPI and TPPI-states methods for quadrature detection in t_1 and t_2 respectively. Zero-filling was employed to yield spectra of 512 (F_1) × 64 (F_2) × 1024 (F_3) points. Additional suppression of the water signal was achieved by convolution of the time-domain data [28,29]. Data were processed either directly on the spectrometer computer or off-line on an SGI Indigo workstation with the program FELIX (Molecular Simulations).

A high-resolution 2D ^1H–^{15}N HSQC experiment [32] was acquired (4096 × 1024 points) to measure the $^3J_{HN-H\alpha}$ coupling constants. For this experiment, protons were not decoupled during the t_2 evolution, thereby allowing ^1H–^1H couplings to evolve during acquisition. The ^1H and ^{15}N carriers were placed at the water frequency and 125.0 p.p.m. respectively, with spectral widths of 3600 Hz (^1H) and 3648 Hz (^{15}N). The O1 for the ^1H dimension was centred within the NH resonance region. The water resonance was folded over in the downfield region of the spectral window. Water was saturated by using phase-shifted square pulses (100 ms for 0.6 s) of 1024 points. The TPPI-states method was used to obtain quadrature detection in both the t_1 and t_2 dimensions. Zero-filling yielded a final spectrum of 4096 × 2048 points.

Structural modelling

Interproton distance constraints were derived from NOEs assigned in 2D ^1H homonuclear and 2D and 3D ^1H–^{15}N heteronuclear-edited NOESY spectra acquired with mixing times of 50, 75, 100 and 200 ms. An analysis of NOE growth curves indicated that, whereas backbone to backbone inter-proton NOEs were normally maximal at 100 ms, side-chain to side-chain and side-chain to backbone NOEs were maximal at 100–200 ms. Generally, by using 75–100 ms NOESY data sets, NOEs were classified as strong, medium, weak or very weak corresponding to upper bound distance constraints of 2.8, 3.3, 4.0 and 4.5 Å respectively. The lower bound restraint between non-bonded protons was set at 1.8 Å. Pseudo-atom corrections were added to the upper-bound distance constraints where appropriate [33] and a 0.5 Å correction was added to the upper bound for NOEs involving methyl protons [34,35]. Averaging was applied to NOEs involving non-stereospecifically assigned methylene protons [36,37]. For $^3J_{HN-H\alpha} > 8$ Hz and $^3J_{HN-H\alpha} < 5$ Hz, the angle ϕ was constrained to be $-120 \pm 40°$ and $-65 \pm 25°$ respectively. The minimum range employed for dihedral angle constraints in ϕ was $\pm 25°$. Stereospecific assignments for β-methylene protons of His-16, Asn-19, Gln-21, Glu-24, Lys-28, His-31, Asn-33, Gln-34, Asp-43, Cys-48, Asp-50 and Asp-52 and for the γ-CH_3 groups of Val-60 were derived from interproton distances obtained from 2D NOESY and 3D ^{15}N-edited NOESY experiments and from qualitative estimates of the magnitude of some $^3J_{H\alpha-H\beta}$ coupling constants obtained from 2D HOHAHA, double-quantum-filtered COSY and 3D ^{15}N-edited HOHAHA experiments. Hydrogen-bond constraints were identified from the pattern of sequential and interstrand NOEs involving NH and CαH protons, together with evidence of slow exchange of protons between amides and solvent. Each hydrogen bond identified was defined by using two distance constraints: $r_{NH-O} = 1.7$–2.3 Å and $r_{N-O} = 2.5$ to 3.3 Å, except for those hydrogen bonds that occur at the ends of secondary structure units, in which $r_{NH-O} = 1.7$ to 2.4 Å and $r_{N-O} = 2.5$ to 3.4 Å.

Derived internuclear distance and angular constraints were used in calculating structures for NAP-2 by using X-PLOR [38].

NAP-2 was created by using parallhdg.pro force fields. For NOE constraints, a soft potential function was used. The first step in our X-PLOR protocol created a template coordinate set by using the Template routine. Then random structures were generated and refined by using the Random and Refine routines respectively. This dynamical simulated annealing procedure ran high-temperature dynamics (2000 K for 50 ps), cooled down (to 100 K in 50 K steps with 1.3 ps molecular dynamics at each temperature step) and energy-minimized the structures. The distance symmetry force constant was kept at 4.2 kJ/mol per Å^2 throughout the calculation. The NOE force constant was doubled at the beginning of each cycle, from an initial value of 2 to a maximum value of 210 kJ/mol per Å^2 while the van der Waals force constant was increased slowly from 0.42 to 16.8 kJ/mol per Å^2. Powell minimization was then performed at 100 K for 250 steps. The resulting structures were subjected to the same Refine routine four times. Significant decreases in E_{total} and E_{NOE} were noted with each Refine cycle. Structures were superimposed by using the BIOSYM INSIGHT viewer and analysed by using X-PLOR analysis routines. Final structures were subjected to the X-PLOR Accept routine with a violation threshold for NOEs of 0.5 Å and dihedral angles of 5 °.

^{15}N–H motional dynamics

^1H_2O samples were used to measure ^{15}N relaxation times. All experiments were performed at 313 K. Relaxation times and ^{15}N-{^{1}H}NOEs were measured by performing the inverse double-INEPT transfer experiments [39]. The time delays for ^{15}N T_1 and T_2 experiments were 0.05, 0.1, 0.15, 0.2, 0.3, 0.4, 0.6 and 0.8 h and 0.007, 0.023, 0.046, 0.069, 0.092, 0.116, 0.139 and 0.162 s respectively. During the Carr–Purcell–Meiboom–Gill sequence in the T_2 experiment, a 400 μs delay was used between the 180 ° ^{15}N pulses to eliminate cross-correlation between dipolar and chemical-shift anisotropy relaxation mechanisms [40–42]. The D and τ delay were set to 0.25J (90 Hz for ^{1}H–^{15}N). Triplicates were performed for each measurement. The transmitter was set in the middle of the NH region and the water resonance was saturated by using phase-shifted square pulses or a Messerle pulse on the water. For ^{15}N-{^{1}H} NOE measurements, experiments were performed with and without proton saturation during the relaxation delay. ^{1}H resonances were saturated by using a train of high-power 120 ° pulses every 5 ms for 3.5 s to build the NOE. In the absence of ^{1}H saturation, a Messerle pulse was used to suppress the water signal before the first ^{15}N pulse, and a 5 s relaxation delay was used between pulses.

To calculate T_1, T_2 and NOE values, peak heights from one-dimensional slices through cross-peaks were measured for the different time delays. Peak intensities decreased exponentially [$I = I_0(e^{-t/T})$] for both T_1 and T_2 data. Regression line analysis was performed, and T_1 or T_2 values were obtained from the line of best fit. NOEs are reported as the ratio $I_{(NOE)}/I_{(ref)}$, where I is the intensity of the resonance. Analysis of these relaxation data is based on the assumption that ^{15}N relaxation is dominated by dipole–dipole interactions with the bonded protons and by chemical-shift anisotropy. In this case, relaxation equations for $R_1 = 1/T_1$, $R_2 = 1/T_2$ and NOE can be written as described by Daragan and Mayo [43]. Contributions from chemical exchange processes, R_{ex}, to R_2 have been included in this analysis.

Relaxation data were analysed by using the Lipari and Szabo [44,45] model free approach, in which it is assumed that the shape of the protein is spherical with an overall correlation time of τ_o and that the internal motions of each NH bond can be described by a correlation time τ_i and an order parameter S^2. For this model, the motional spectral density function can be written [44,45]:

$$J(\omega) = S^2\tau_o/(1+\omega^2\tau_{o*2}) + (1-S^2)\tau/(1+\omega^2\tau^2) \quad (1)$$

where $1/\tau = 1/\tau_o + 1/\tau_i$. The overall correlation time τ_o was initially estimated by minimizing the following target function:

$$F_{error} = [(R_{1,obs} - R_{1,calc})/R_{1,obs}]^2 + [(R_{2,obs} - R_{2,calc})/R_{2,obs}]^2 + [(NOE_{obs} - NOE_{calc})/NOE_{obs}]^2 \quad (2)$$

for each residue separately. $R_{1,obs}$, $R_{2,obs}$ and NOE_{obs} are experimental values; $R_{1,calc}$, $R_{2,calc}$ and NOE_{calc} are calculated values. In a subsequent minimization, an average value of τ_o was used with only R_1 and NOE, and τ_o, τ_i and S^2 were varied to minimize the target function. R_2ex values were then essentially calculated from the difference of observed and calculated values for R_2. Inclusion of these values in the analysis generally improved overall fits.

RESULTS AND DISCUSSION

Resonance assignments

Monomeric NAP-2 was generated by adding to the solution 4 % (v/v) 2-chloroethanol, which is known to dissociate the dimeric and tetrameric aggregation states of the protein [19,20]. Because ^{1}H-NMR sequence-specific assignments for monomeric NAP-2 are known [19], heteronuclear ^{1}H–^{15}N 2D-NMR and 3D-NMR experiments were performed to acquire ^{15}N resonance assignments and additional NOE distance constraints and motional dynamics information. For uniformly ^{15}N-enriched NAP-2, a ^{1}H–^{15}N HSQC 2D-NMR contour plot is shown in Figure 1. ^{1}H–^{15}N sequence-specific resonance assignments labelled in Figure 1 have been derived by starting with known ^{1}H resonance assignments [19] and following connectivities through ^{15}N-edited HOHAHA and NOESY 3D-NMR spectra (results not shown).

Solution structure

Elements of secondary structure have been deduced from a qualitative interpretation of ^{1}H NOEs, $^3J_{\alpha N}$ coupling constants and long-lived backbone NH groups [19]. In that study, outside the β-sheet domain, few long-range side-chain to side-chain NOEs could be identified given the fact that NAP-2 contains only one tyrosine residue and two histidine residues and a preponderance of aliphatic hydrophobic residues. It is these NOEs that best define overall folding. For NAP-2 the derivation of secondary structural elements was therefore limited to folding within the β-sheet and α-helix domains [19]. In ^{1}H–^{15}N NOESY 3D-NMR experiments, significant numbers of side-chain to backbone NOEs could be identified. In particular, several NOEs between the hydrophobic faces of the amphipathic β-sheet and C-terminal α-helix were observed for use in modelling studies.

A total of 858 NOE distance constraints were derived from an analysis of both homonuclear and heteronuclear NOESY spectra. These included 420 intra-residue, 148 sequential, 123 medium-range ($|i-j| < 5$) and 167 long-range ($|i-j| \geq 5$) constraints. In addition, torsion angle constraints were obtained for 42 values of ϕ. A total of 16 hydrogen bonds were identified from long-lived backbone NH groups and by inspection of initial NAP-2 structures, giving rise to 32 hydrogen-bond distance constraints. These hydrogen-bond constraints account for the slowly exchanging amide protons identified. The total number of experimentally derived constraints was therefore 932, giving a total of approx. 13 constraints per residue.

Initially, 100 structures for NAP-2 were calculated as described in the Materials and methods section. The best-fit superpositions

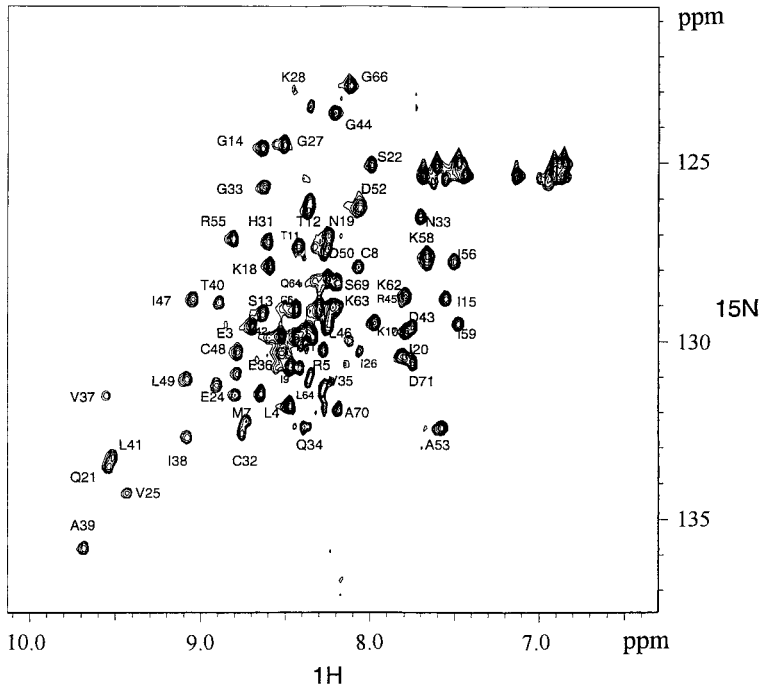

Figure 1 ^{15}N–^{1}H HSQC of NAP-2

A ^{15}N-^{1}H HSQC contour plot for NAP-2 in the 2-chloroethanol-induced monomer state is shown. This 2D-NMR data set was acquired as discussed in the Materials and methods section. Cross-peaks are labelled with sequence-specific resonance assignments.

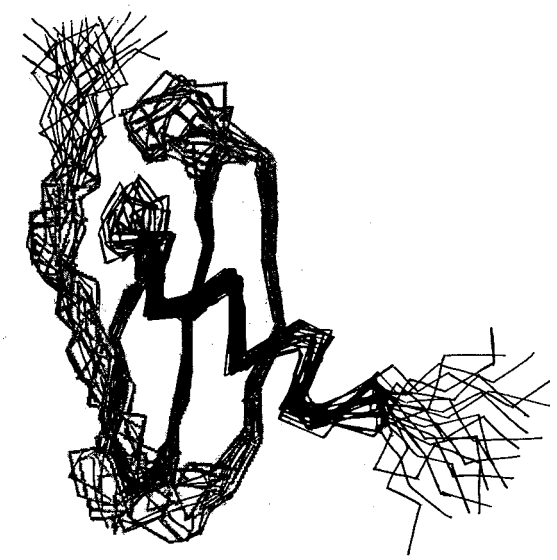

Figure 2 Structure of monomeric NAP-2

Structures for monomeric NAP-2, based primarily on NOEs, were calculated as discussed in the Materials and methods section. The β-sheet domains of 20 structures were superimposed.

of backbone Cα atoms for the final 20 structures, along with an average structure, are shown in Figure 2. These structures showed no NOE violations greater than 0.5 Å [46]. Structural statistics are summarized in Table 1. The less structurally defined N-terminus and the end of the C-terminal helix are apparent. The structures satisfy experimental constraints quite well. Excluding N-terminal residues 1–5 and C-terminal residues 66–72, which are least well defined by the data, atomic root-mean-square (RMS) differences with respect to the mean coordinate positions are 0.63 ± 0.07 Å for backbone (N, Cα, C) atoms and 1.5 ± 0.3 Å for all heavy atoms. For the three β-sheet strands (Gln-21–Lys-28, Gln-34–Thr-40 and Lys-46–Leu-49) as well as for the loop connecting strands 2 and 3 (Leu-41–Arg-45), the average backbone RMS deviation is 0.38 Å. In addition, ϕ and ψ angular order parameters are all more than 0.8. The angular order parameter is defined such that a value of 1 indicates an exactly defined angle and a value of 0 results from complete dihedral heterogeneity [47]. Backbone torsion angles for all non-glycine residues lie within the allowed region of a Ramachandran ϕ–ψ plot. Taken together, the above data indicate that these structures used to represent the solution conformation of NAP-2 are well converged.

Even though the C-terminal helix in itself is structurally well defined, the position of the C-terminal helix on top of the β-sheet domain could not be established initially [19] owing to a lack of inter-domain NOEs resulting from the presence of only hydrophobic aliphatic residues lying between the helix and the sheet. Use of ^{15}N-edited 2D-NMR and 3D-NMR experiments, however, has allowed a number of these constraints to be identified. Residues Ile-56, Ile-59, Val-60, Leu-64 and Ala-65 at the top of the helix interact with β-sheet residues Leu-23, Val-25, Val-35, Val-37, Ala-39 and Leu-41. In the crystal, NAP-2 forms tetramers; the X-ray structure shows that the C-terminal helix is uniquely positioned, with the same inter-domain contact residues [19].

The overall structural folding of monomeric NAP-2 is generally conserved relative to other α-chemokines such as IL-8 [24,48,49], Gro-α [50], bovine PF4 [21] and human PF4 [22,23]. Significant

Table 1 Structural statistics

None of the 20 final structures exhibited distance restraint violations greater than 0.5 Å or dihedral angle violations greater than 5 °. RMS deviations are means ± S.D. for the 20 structures. The final values of the NOE (E_{NOE}), torsion angle (E_{CDIH}) and NCS (E_{NCS}) potentials were calculated with force constants of 210 kJ/mol per Å^2, 840 kJ/mol per rad^2 and 126 kJ/mol per Å^2 respectively.

Parameter	RMS deviation from experimental distance restraints (Å)
NOE (858 per monomer)	0.06 ± 0.0035
Hydrogen bond (32 per monomer)	
Parameter	**Deviation from idealized geometry**
Bonds (Å)	0.004
Angles (degrees)	0.69 ± 0.03
Impropers (degrees)	0.6 ± 0.03
Parameter	**Energy (kJ/mol)**
E_{NOE}	67.2 ± 8.4
E_{CDIH}	12.6 ± 2.94
E_{NCS}	16.8 ± 4.2
E_{BOND}	33.6 ± 4.2
E_{ANGLE}	205.8 ± 33.6
$E_{IMPROPER}$	6.3 ± 8.4
E_{TOTAL}	399 ± 46.2

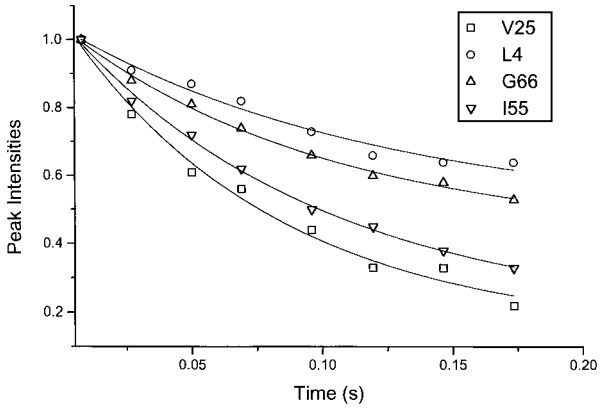

Figure 4 ^{15}N relaxation decay curves for NAP-2

Four representative ^{15}N T_1 decay curves are shown for monomeric NAP-2: □, Val-25; ○, Leu-4; △, Gly-66; ▽, Ile-55. Peak intensities were derived from slices through cross-peaks as discussed in the text.

structural differences, however, can be noted in loop/turn sequences and in N-terminal and C-terminal domains. Backbone atomic RMS deviations calculated from a best-fit superposition between β-sheet residues of NAP-2, IL-8 and PF4 range from 0.35 to 1.1 Å. For loop residues 28–34 and 50–54, RMS deviations are significantly increased. C-terminal residues 55–67 are well defined within themselves, but in this comparison showed 0.8–1.6 Å deviations for residues 55–63 and 2.8–3.5 Å deviations for residues 64–67. These later deviations reflect differences in quaternary structure and the fact that structural superpositions were optimized for β-sheet residues. For the same reasons, N-terminal residues also show large RMS deviations. In PF4 and NAP-2, the C-terminal helix runs for 11 and 13 residues respectively, whereas in IL-8 it runs for 18 residues. For IL-8 and PF4, this helix extends to the final C-terminal residue, whereas for NAP-2 Gly-66 and Asp-67 give considerably weaker inter-residue helix NOEs, and the paucity of NOEs within the last five potential helical residues suggests significant internal mobility of the NAP-2 C-terminus in the monomeric state. In tetrameric PF4 [22] and dimeric IL-8 [48], the final C-terminal residue in one subunit is anchored via inter-residue electrostatic interactions with an opposing subunit. Even in the X-ray crystal structure of tetrameric NAP-2 [18], the C-terminal helix is well defined throughout. These observations indicate that subunit associ-

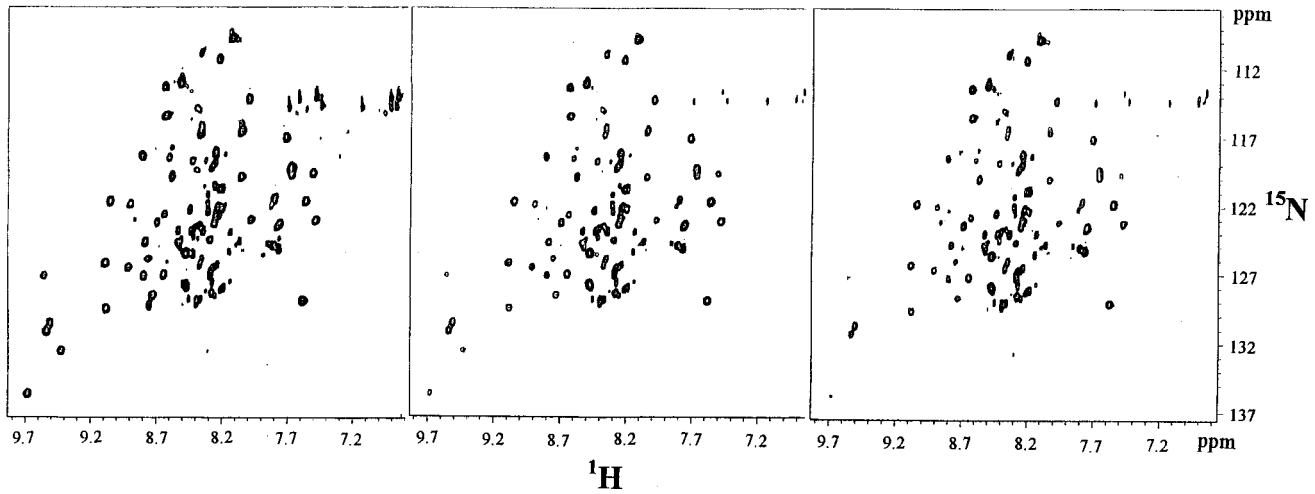

Figure 3 ^{15}N–^{1}H HSQC relaxation spectra of NAP-2

A series of three ^{15}N–^{1}H HSQC relaxation spectra for NAP-2 are shown. The delay times, T_2, for these plots were 7.7 ms (left panel), 96 ms (middle panel) and 173.5 ms (right panel). The acquisition of these 2D-NMR data sets was as discussed in the Materials and methods section.

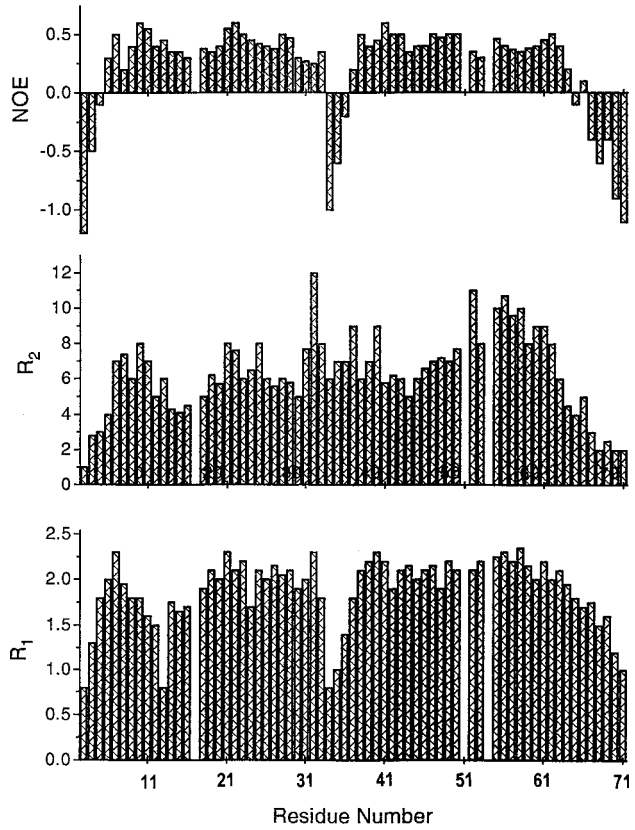

Figure 5 ^{15}N R_1, R_2 and NOE values for NAP-2

^{15}N R_1, R_2 and NOE values for monomeric NAP-2 are plotted in bar graph format against the NAP-2 sequence. Values were derived as discussed in the text. Results shown are averages of two separate measurements; standard deviations (results not shown) were on average ±15% for R_1, ±25% for R_2 and ±20% for NOE.

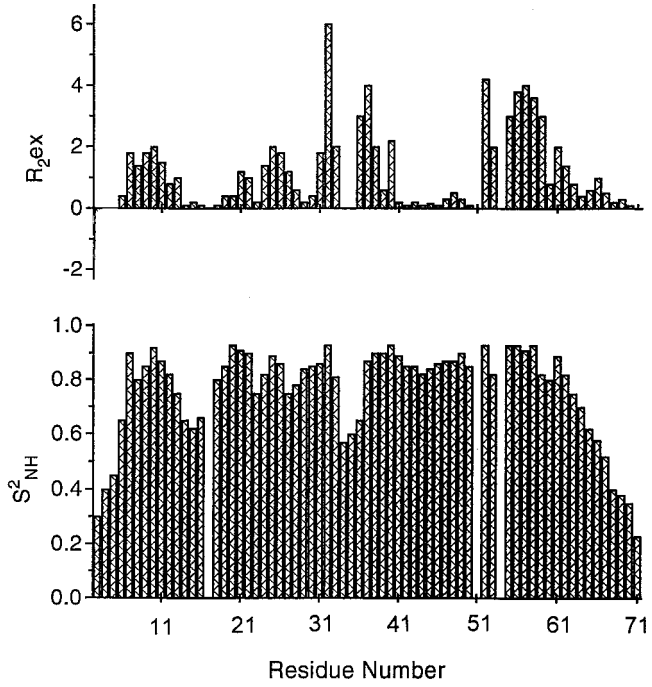

Figure 6 Motional order parameters and exchange terms for NAP-2

Motional order parameters, S^2_{NH}, and conformational exchange terms, R_2ex, are plotted against the NAP-2 sequence. Values were derived as discussed in the text.

ations in NAP-2 (and in other α-chemokines) stabilize the C-terminal helix conformation with respect to the β-sheet domain. This in turn suggests that subunit association might also dampen internal flexibility in general in NAP-2.

^{15}N–H backbone dynamics

^{15}N T_1 and T_2 relaxation times and ^{15}N-{^{1}H} NOEs were measured as described in the Materials and methods section. A series of three time-modulated ^{1}H–^{15}N 2D-NMR spectra are shown in Figure 3 to exemplify changes in cross-peak intensities resulting from differential ^{15}NH relaxation rates. T_1, T_2 and NOE values were calculated by measuring peak heights from one-dimensional slices through cross-peaks for the different time delays. Peak intensities decreased exponentially [$I = I_o(e^{-t/T})$] for both T_1 and T_2 data as exemplified by T_1 data shown in Figure 4. The solid line through data points represents the line of best fit from regression analysis. Experimental ^{15}N R_1, R_2 and NOE values are plotted against the NAP-2 residue number in Figure 5.

Using the Lipari and Szabo model free approach [44,45] and the minimization procedure described in the Materials and methods section, the best value for the overall correlation time, τ_o, was 3.7 ns. In terms of the dependence of τ_o on the number of residues in a protein, this value for monomeric NAP-2 compares reasonably well with τ_o values of other proteins obtained by using NMR relaxation [43]. The average internal correlation time was 170 ps. ^{15}N motional order parameters, S^2_{NH}, along with R_2 chemical exchange terms, R_2ex, are plotted against the NAP-2 residue number in Figure 6. Inclusion of the Rex exchange term generally improves the fit in the model free analysis of the data. S^2_{NH} values range from approx. 0.3 at the termini to 0.3–0.7 with some loops/turns to 0.8–0.93 within the β-sheet and helix domains. Order parameters generally decrease at the termini, as expected for more mobile segments. A value of 0.3 is close to unrestricted motion. To check that R_2ex does indeed result from conformational exchange and not from anisotropy, relaxation data were acquired at two spectrometer frequencies (500 and 600 MHz). In all cases, the ratio between the relaxation terms at 600 and 500 MHz fell between 1.4 and 1.5, which is around the expected value of 1.44, indicating that R_2ex results from conformational exchange. R_2ex values range from 0 to approx. 6. A larger R_2ex value indicates greater contributions from conformational exchange on the millisecond time scale. The significance of R_2ex values was gauged by averaging all R_2ex values to yield a threshold value of 1.1. Given an experimental error of approx. 10% in determining R_2, this R_2ex threshold value is greater than the actual error in any R_2ex value. Even using this threshold value, R_2ex values for residues 7–11, 24–26, 31–33, 36–40 and 52–61 remain significant.

In terms of S^2_{NH} and R_2ex, three main classifications for internal motions in NAP-2 can be devised: case 1, low S^2_{NH} (less than approx. 0.6–0.7) with R_2ex below threshold; case 2, high S^2_{NH} (greater than 0.7) with R_2ex below threshold; and case 3, high S^2_{NH} (greater than 0.7) with R_2ex above threshold. Case 1 defines the situation in which backbone internal motions and conformational exchange (chemical shift time scale) are relatively fast as observed at N-termini and C-termini and within segments Gly-14–His-16 and Gln-34–Val-35. Case 2 defines the situation in which backbone internal motions occur slowly on the R_1 time

scale and conformational exchange on the chemical-shift time scale is not apparent. Segments Gly-27–Thr-30 and Leu-41–Asp-50 fall into this category. This latter stretch of the sequence includes the α-chemokine folding initiation site (Leu-41–Arg-45) [51] and contains many of the longest lived NH groups consistent with its position at the core of the protein. Structurally, this is one of the best defined regions in NAP-2. Finally, case 3 defines the situation in which the structure is well defined but internal motions occur on the millisecond chemical-shift time scale. Sequences that fall within this motional time regime include Met-7–Thr-11, Glu-24–Ile-26, His-31–Asn-33, Glu-36–Thr-40 and Asp-52–Gln-61. Structurally, the respective sequences are at the N-terminus, the end of β-strand 1, the loop between strands 1 and 2, β-strand 2 and the end of β-strand going into the C-terminal α-helix, and all are proximal to each other in the structure (see Figure 2).

The overall structural dynamics picture of NAP-2 is a that of an aperiodic, highly mobile N-terminal segment that leads into a well-defined β-sheet scaffold on which is folded a C-terminal helix. Fast N-terminal motions are apparently slowed by Cys-6 and Cys-8, which form disulphide bridges to Cys-32 and Cys-48 respectively. Even these bridged sequences, however, are flexible on the millisecond chemical-shift time scale; note that Cys-32 displays the largest R_2ex value. These slower motions continue from Ile-9 to Thr-12, probably as the result of this sequence's being close to disulphide bond-constrained Cys-6 and Cys-8 and the fact that Thr-11 and Thr-12 form a very short β-sheet with Lys-46–Leu-49. The next four residues, Ser-13–His-16, show increased mobility. In general the aperiodic N-terminus in NAP-2 is inherently flexible and is constrained only in specific places when stabilized by interactions with the β-sheet. On the C-terminal side of Pro-17 leading into the first β-sheet strand, motions are more attenuated. Near the middle of this first strand and into the large inter-strand loop (residues Ile-26, Gly-27, Lys-28, Gly-29 and Thr-30), motions remain dampened; this is somewhat surprising because two glycine residues are contained within this short sequence. On the C-terminal side of Cys-32, mobility is greater from Gln-34 to Glu-36, less within the latter part of β-sheet strand 2, residues Val-37–Thr-40, and less still on entering the folding initiation turn sequence through the third β-sheet strand up to Leu-49–Asp-50. Pro-51 and Pro-54 form a loop/turn that initiates the C-terminal α-helix. The initial part of this helix from Ile-56 to about Lys-63 undergoes relatively slow conformational exchange, which is increased to the fast-exchange regime on moving towards the C-terminus. This slower conformational exchange within the well-structured top part of the helix is also noted within the first two strands of the β-sheet within which it is sandwiched by a number of hydrophobic aliphatic residues mentioned above. IL-8, which contains several aromatic residues between the helix and the sheet, seems to have a more stable structure. Furthermore, in solution IL-8 is a dimer [48] whose structural stability is enhanced by interactions of the end of the C-terminal helix from one subunit with an opposing subunit. The end of the C-terminal helix in NAP-2 monomers is fully solvent-exposed and forms a transient helix. This is consistent with the structural analysis of NAP-2, which showed few intra-helix NOEs from Asp-67 to Tyr-72.

Conclusions

The NMR solution structure of monomeric NAP-2 is essentially the same as that found in other α-chemokines with a three-stranded anti-parallel β-sheet on which is folded a C-terminal α-helix and an aperiodic N-terminal sequence. Dissociation to the monomeric state, however, increases internal mobility owing to a loss of stabilizing inter-subunit interactions. The present study emphasizes the fact that when elucidating protein structures in solution (or in the crystal), it is important to take into account internal motions to have a more complete picture of the physical state of a structure.

This work was supported by research grants from the American Heart Association, both National (no. 96006050) and Minnesota Affiliate and from Repligen Corp. (Boston, MA, U.S.A.).

REFERENCES

1 Walz, A., Dewald, B., von Tscharner, V. and Baggiolini, M. (1989) J. Exp. Med. **170**, 1745–1750
2 Holt, J. C., Harris, M. E., Holt, A., Lange, E., Henschen, A. and Niewiarowski, S. (1986) Biochemistry **25**, 1988–1996
3 Castor, C. W., Miller, J. W. and Walz, D. A. (1983) Proc. Natl. Acad. Sci. U.S.A. **80**, 765–769
4 Begg, G. S., Pepper, D. S., Chesterman, C. N. and Morgan, F. J. (1978) Biochemistry **17**, 1739–1744
5 Deuel, T. F., Keim, P. S., Farmer, M. and Heinrikson, R. L. (1977) Proc. Natl. Acad. Sci. U.S.A. **74**, 2256–2258
6 Mire-Slius, A. and Thorpe, R., eds. (1998) Cytokines, Academic Press, San Diego
7 Schmid, J. and Weissmann, C. (1987) J. Immunol. **139**, 250–256
8 Anisowicz, A., Bardwell, L. and Sager, R. (1987) Proc. Natl. Acad. Sci. U.S.A. **84**, 7188–7192
9 Schnitzel, W., Garbeis, B., Monschein, U. and Besemer, J. (1991) Biochem. Biophys. Res. Commun. **18**, 301–307
10 Moser, B., Schumacher, C., von Tscharner, V., Clark-Lewis, I. and Baggiolini, M. (1991) J. Biol. Chem. **266**, 10666–10671
11 Schumacher, C., Clark-Lewis, I., Baggiolini, M. and Moser, B. (1992) Proc. Natl. Acad. Sci. U.S.A. **89**, 10542–10546
12 Holt, J. C., Yan, Z. O., Lu, W. Q., Stewart, G. J. and Niewiarowski, S. (1992) Proc. Soc. Exp. Biol. Med. **199**, 171–177
13 Yang, Y., Mayo, K. H., Daly, T. J., Barry, J. K. and La Rosa, G. L. (1994) J. Biol. Chem. **269**, 20110–20118
14 Mayo, K. H. and Chen, M. J. (1989) Biochemistry **28**, 9469–9478
15 Mayo, K. H. (1991) Biochemistry **30**, 925–934
16 Rajarathnam, K., Sykes, B. D., Kay, C. M., Dewald, B., Geiser, T., Baggiolini, M. and Clark-Lewis, I. (1994) Science **264**, 90–92
17 Rajarathnam, K., Kay, C. M., Dewald, B., Baggiolini, M., Clark-Lewis, I. and Sykes, B. D. (1997) J. Biol. Chem. **272**, 1725–1729
18 Malkowski, M. G., Wu, J. Y., Lazar, J. B., Johnson, P. H. and Edwards, B. F. P. (1995) J. Biol. Chem. **270**, 7077–7087
19 Mayo, K. H., Yang, Y., Daly, T. J., Barry, J. K. and LaRosa, G. J. (1994) Biochem. J. **304**, 371–376
20 Yang, Y., Barker, S., Chen, M.-J. and Mayo, K. H. (1993) J. Biol. Chem. **268**, 9223–9229
21 St. Charles, R., Walz, D. A. and Edwards, B. F. P. (1989) J. Biol. Chem. **264**, 2092–2099
22 Zhang, X., Chen, L. and Bancroft, D. P. (1994) Biochemistry **33**, 8361–8366
23 Mayo, K. H., Roongta, V., Ilyina, E., Milius, R., Barker, S., Quinlan, C., La Rosa, G. and Daly, T. J. (1995) Biochemistry **34**, 11399–11409
24 Clore, G. M., Appella, E., Yamada, M., Matsushima, K. and Gronenborn, A. M. (1990) Biochemistry **29**, 1689–1696
25 Crump, M. P., Gong, J. H., Loetscher, P., Rajarathnam, K., Amara, A., Arenzana-Seisdedos, F., Virelizier, J. L., Baggiolini, M., Sykes, B. D. and Clark-Lewis, I. (1997) EMBO J. **16**, 6996–7007
26 Myers, J. A., Gray, G. G., Peters, D. J., Grimaila, R. J., Hunt, A. J., Maione, T. E. and Muellar, W. T. (1991) Protein Express. Purif. **2**, 136–143
27 Smith, P. K., Krohn, R. I., Hermanson, G. T., Mallia, A. K., Gartner, F. H., Provenzano, M. D., Fujimoto, E. K., Goeke, N. M., Olson, B. J. and Klenk, D. C. (1985) Anal. Biochem. **150**, 76–85
28 Marion, D., Driscoll, P. C., Kay, L. E., Wingfield, P. T., Bax, A., Gronenborn, A. M. and Clore, G. M. (1989) Biochemistry **28**, 6150–6156
29 Marion, D., Kay, L. E., Sparks, S. W., Torchia, D. A. and Bax, A. (1989) J. Am. Chem. Soc. **111**, 1515–1517
30 Driscoll, P. C., Clore, G. M., Marion, D., Wingfield, P. T. and Gronenborn, A. M. (1990) Biochemistry **29**, 3542–3556
31 Fesik, S. W. and Zuiderweg, E. R. P. (1990) Quart. Rev. Biophys. **23**, 97–131
32 Bodenhausen, G. and Ruben, D. J. (1980) Chem. Phys. Lett. **69**, 185–189
33 Wüthrich, K., Billeter, M. and Braun, W. (1983) J. Mol. Biol. **169**, 949–961

34 Tropp, J. (1980) J. Chem. Phys. **72**, 6035–6043
35 Koning, T. M. G., Boelens, R. and Kaptein, R. (1990) J. Magn. Reson. **90**, 111–123
36 Brunger, A. T., Clore, G. M., Gronenborn, A. M. and Karplus, M. (1986) Proc. Natl. Acad. Sci. U.S.A. **83**, 3801–3805
37 Clore, G. M., Brunger, A. T., Karplus, M. and Gronenborn, A. M. (1986) J. Mol. Biol. **191**, 523–551
38 Brunger, A. T. (1992) X-plor Manual, Yale University Press, New Haven
39 Barbato, G., Ikura, M., Kay, L. E., Pastor, R. W. and Bax, A. (1992) Biochemistry **31**, 5269–5278
40 Boyd, J., Hommel, U. and Campbell, I. D. (1990) Chem. Phys. Lett. **175**, 477–482
41 Kay, L. E., Nicholson, L. K., Delaglio, F., Bax, A. and Torchia, D. A. (1992) J. Magn. Reson. **97**, 359–375
42 Palmer, A. G., Skelton, N. J., Chazin, W. J., Wright, P. E. and Rance, M. (1992) Mol. Phys. **75**, 699–711
43 Daragan, V. and Mayo, K. H. (1997) Prog. NMR Spectrosc. **31**, 63–105
44 Lipari, G. and Szabo, A. (1982) J. Am. Chem. Soc. **104**, 4546–4559
45 Lipari, G. and Szabo, A. (1982) J. Am. Chem. Soc. **104**, 4559–4570
46 Nilges, M. (1993) Proteins Struct. Funct. Genet. **17**, 297–309
47 Hyberts, S., Goldberg, M. S., Havel, T. F. and Wagner, G. (1992) Protein Sci. **1**, 736–751
48 Clore, G. M., Bax, A., Wingfield, P. T. and Gronenborn, A. M. (1990) Biochemistry **29**, 5671–5676
49 Baldwin, E. T., Weber, I. T., St. Charles, R., Xuan, J.-C., Appella, E., Yamada, M., Matsushima, K., Edwards, B. F. P., Clore, G. M., Gronenborn, A. M. and Wlodawer, A. (1991) Proc. Natl. Acad. Sci. U.S.A. **88**, 502–506
50 Fairbrother, W. J., Reilly, D., Colby, T. J., Hesselgesser, J. and Horuk, R. (1994) J. Mol. Biol. **242**, 252–270
51 Ilyina, E., Milius, R. and Mayo, K. H. (1994) Biochemistry **33**, 13436–13444

Received 11 May 1998/4 January 1999; accepted 12 January 1999